Hu Z, Gallacher B.

Precision Mode Tuning Towards a Low Angle Drift MEMS Rate Integrating Gyroscope.

***Mechatronics* (2017)**

DOI: https://doi.org/10.1016/j.mechatronics.2017.04.007

Precision Mode Tuning Towards a Low Angle Drift MEMS Rate Integrating Gyroscope

Zhongxu Hu, Barry J Gallacher

School of Mechanical and System Engineering, Newcastle University, Newcastle upon Tyne, UK

Abstract:

This paper describes a high precision mode tuning scheme for a MEMS vibratory gyroscope operating in the rate integrating mode (RIG). The tuning scheme minimizes both the cross and diagonal imperfection components in the stiffness matrix. It consists of "coarse" and "fine" tuning stages respectively conducted in rate mode and rate integrating mode. The first stage of mode tuning in the rate mode is automated and can be completed within a few minutes with an accuracy of a few tens of mHz. The tuning accuracy at this stage is restricted by the damping imperfections that distort the phase response as the stiffness imperfections are reduced. Further improvement to the tuning accuracy is achieved at the second stage by switching the gyro to operate in the rate integrating mode, where the influence of damping imperfections on the tracked resonance frequency is negligible when the amplitude of the minor axis of the elliptical trajectory of the vibration is minimized. Accurate assessments of the stiffness imperfections are made by deliberate angle precession and examining the tracked resonant frequency variation from the average resonance frequency at certain angular locations. A tuning accuracy of 10 mHz is achieved while the gyroscope is operated in whole angle mode. Minimum frequency mismatch is a great advantage for the closed-loop control of the rate integrating gyroscope, such as quadrature nulling and phase locked loop based frequency tracking. Angle error is also reduced as a consequence.

Keywords:

Rate integrating gyroscope; Mode tuning; Low angle drift.

1. Introduction

In recent years, affordable and integrated MEMS Coriolis vibratory gyroscopes (CVGs) have found increasing usages in compact and low cost inertial applications where they can replace expensive and bulky fibre optical (FOG) or mechanical macro scale gyro. Examples include the attitude and heading reference system (AHRS) in UAV navigation and the position and orientation system (POS) for mobile mapping. The working principle of a CVG is based on energy transfer caused by the Coriolis coupling between a pair of degenerate vibration modes associated with axisymmetric structures. Common examples include string[1], tuning fork[2], ring [3][4], cylinder[5], disk[6][7][8] and hemispherical shell[9][10]. Among these structures, the ring resonator is particularly suitable for MEMS fabrication because of its planar topology. Most MEMS gyroscopes operate in rate mode, though they can be operated in rate integrating mode (RIG) that directly give precession angle without the need of digital integration. Other advantages of RIGs include: (1), scale factor stability unaffected by environment changes and amplitude of vibration of the drive mode; (2), unlimited bandwidth and measurement range, though, this benefit may be compromised by bandwidth of the electronic control loops [3].

Recently, as the technology of microfabrication advances, MEMS RIGs have become the subject of significant research [11][12][13][14]. The major performance specifications for RIG are the precession angle dependent bias error and the minimum rate threshold [15][16]. They are mainly affected by damping and stiffness imperfections caused by fabrication tolerance limits and material inhomogeneity. Drive and sensing electrode misalignments, gain mismatches of the resonance modes, and phase errors in the feedback control signals also contribute to the total angle drift [17]. In the development of high performance RIGs, matching the two vibration

modes is the first obstacle to overcome. It is advantageous to be able to minimize the frequency mismatch prior to any specific compensation based on state feedback control, in the sense that it reduces the required control forces for nulling the quadrature amplitude and avoids the undesirable side effects of these control forces.

Various tuning and calibration methods for mode correction have been reported in the past. Passive post-fabrication trimming methods, such as laser trimming, ion beam milling and mass loading by selective deposition [18][19] have been used in high end macro-scale vibratory gyroscopes, such as the HRG and disk gyroscope [7] to reduce the anisotropy. However, this type of tuning is inflexible, time consuming and therefore significantly increases the cost of the gyro.

Active mode tuning, mainly electrostatic, is widely used in high performance MEMS gyroscopes. It uses electrostatic spring softening effect to change the stiffness matrix of the system dynamics [20][21][22][23]. It provides greater flexibility, relatively large tuning range in comparison to state feedback [24], and the possibility of on-line electrostatic mode tuning during operation against slow parameter variation induced by temperature changes, aging and other environmental influences. It is possible to design a closed loop automatic tuning procedure for rapid mode tuning. For example, Oboe [25] proposed a real-time tuning mechanism that electrostatically detunes the sense mode until the amplitude of the sense mode vibration caused by residual cross coupling is maximized. This closed loop control appears as an optimization problem by extreme-seeking. Accuracy up to 0.1Hz was achieved from these closed loop tuning schemes. Akin [26] proposed a closed loop mode matching control that regulates the electrostatic tuning voltages, so that the sense mode output in response to a dither signal is in phase with that of the drive mode, indicating matched modes. To avoid interfering with the input rotation rate, Prikhodko [27] proposed an improved real time automatic mode tuning by applying a dither signal that is typically outside of the gyroscope bandwidth. The disadvantage of electrostatic mode tuning is that the nonlinear relationship between tuning voltages and the electrostatic stiffness can adversely affect the stability and bandwidth of real time electrostatic tuning.

Real–time feedback control [24][28] have been used in dynamic compensation of mechanical imperfection or parameter uncertainty. Park [28] proposed an adaptive add-on control with a parameter adaptation algorithm that provides an estimate of the angular rate and quadrature error simultaneously. However, robustness and bandwidth of the adaptive algorithm is of concern in practical gyroscope control system. The limitation of feedback control based mode tuning is the small tuning range. Often feedback control is used as a dynamic compensation after a “coarse” electrostatic tuning procedure.

So far, most of the reported mode tuning schemes don’t consider the influences of damping imperfections. For example, cross damping contributes to the residual output at the sense mode. Cross damping affects its phase angle, and therefore limits the precision of mode tuning. When the gyroscope tuned in rate mode is operated in the RIG mode, it is very common that the modes appear well tuned at one angular location, but detuned when the standing wave starts to precess due to rate input. On the other hand, a gyroscope tuned in RIG mode still remains tuned when it is operated in rate mode. In the rate operating mode, the quadrature component at the sense mode output, or the phase information of the secondary mode relative to the drive mode is used as an effective indirect measurement of mistuning. Similarly, in the angle operation mode, the quadrature amplitude, which refers to the amplitude of the minor axis of the elliptical vibration trajectory, is an effective control criterion (to be minimized) for dynamic compensation of stiffness imperfections [12].

This paper presents a high precision mode tuning scheme for a MEMS ring type CVG. It has unique electrode arrangement that maximizes electromechanical coupling. A decoupling algorithm is established to provide independent tuning of both the cross and diagonal terms of the stiffness matrix. The whole tuning consists of two stages. Firstly electrostatic tuning of the gyro operating in rate mode is used to rapidly remove the major part of stiffness cross coupling and mistuning. It is designed in a closed-loop form that first minimizes the total cross coupling from the drive mode, and then minimizes the quadrature component of the sense mode when a pilot rate input is applied to the sense mode. Mistuning achieved at this stage can be assessed simply using the

ratio between the in-phase and the quadrature components of the sense mode output [20]. However, precise calculation of mistuning is hindered by the inevitable coupling caused by damping. Electrostatic trimming cannot remove the effect of damping imperfections. At the secondary stage, the electrostatically tuned gyro is controlled to operate in rate integrating mode. The amplitude of quadrature component described by the minor axis of the elliptical trajectory is suppressed to near zero. At this stage the influence of damping imperfections on the tracked resonance frequency are negligible. The controlled RIG is able to respond to a constant rate input as low as 15 degrees per second and precess continuously. It is convenient to separate the influences of the two stiffness components on the tracked resonance frequency by examining the resonance frequency deviation from the average at certain angular locations. Further electrostatic trimming or state feedback is then applied to eliminate the residual mistuning. The mode matched RIG shows 10 mHz frequency split under full rotation.
The contributions of this paper are threefold: (1) A rapid closed-loop form "coarse" mode tuning using the phase information based on the transfer function model of the CVG; (2) High precision mode tuning by removing the influence of non-proportional damping on tracked resonance frequency in rate integrating mode; (3) Direct assessment of frequency mismatch. The rest of the paper is organized as follows: The transfer function model and time average model for the CVGs are presented in section 2, on which the principles for the closed loop "coarse" mode tuning and "fine" mode trimming are based respectively. A brief description of electrostatic spring softening and a simple decoupling algorithm for individual trimming of the cross and diagonal components of the stiffness matrix is provided in section 3. The algorithms and tuning procedures for the "coarse" and "fine" tuning stages are presented in section 4 and 5 respectively. Detailed experimental results are provided in section 6 for validation of this tuning scheme.

2. The gyroscope and its equations of motion

This section presents the two types of motion equation of the vibratory gyroscope. Two different coordinate systems will be used in order to make the control strategy clear. A rectangular coordinate system aligned with the drive and sensing electrodes will be used for the "coarse" mode tuning. The time averaged dynamics are best presented in an elliptic coordinate system and will be used for the "fine" mode tuning.
The structure of the single-axis ring vibratory gyroscope and a packaged sample device are shown in Figure 1. The vibrating structure for gyroscopic sensing is a suspended ring, which has a radius of 4mm, width of 200um and thickness of 150um. The capacitive gap formed between the ring and the electrodes is 10um, which gives a quiescent capacitance of 0.96pF. The device is fabricated from silicon <111> by Silicon Sensing. Eight section electrodes are situated outside of the ring structure providing balanced electrostatic excitation (PD and SD) and differential capacitive sensing (PPO and SPO) of the in-plane flexural motion of vibration. The acronyms PD, SD refer to the primary mode and secondary mode drive electrodes, and PPO and SPO refer to primary mode and secondary mode pickoff electrodes respectively. There are 16 tuning electrodes connected into four groups (PCW, PACW, SCW and SACW) located inside of the ring providing electrostatic correction of the stiffness matrix of the resonator. The acronyms PCW, PACW refer to the primary mode tuning electrodes rotated clockwise or anticlockwise relative to the primary mode drive electrode PD. Similarly, the acronyms SCW, SACW refer to the secondary mode tuning electrodes rotated clockwise or anticlockwise relative to the secondary mode drive electrode SD. Each group has four evenly placed tuning electrodes along the circumferential of the ring. This electrode arrangement has the advantage of increased electromechanical coupling factor for both excitation and sensing, and maximum electrostatic tuning range from using the whole interior space of the ring. A disadvantage of this electrode configuration is that the four tuning voltages are coupled in the correcting stiffness matrix, which requires decoupling algorithm so that independent modification of the cross and diagonal terms of the stiffness matrix is possible.

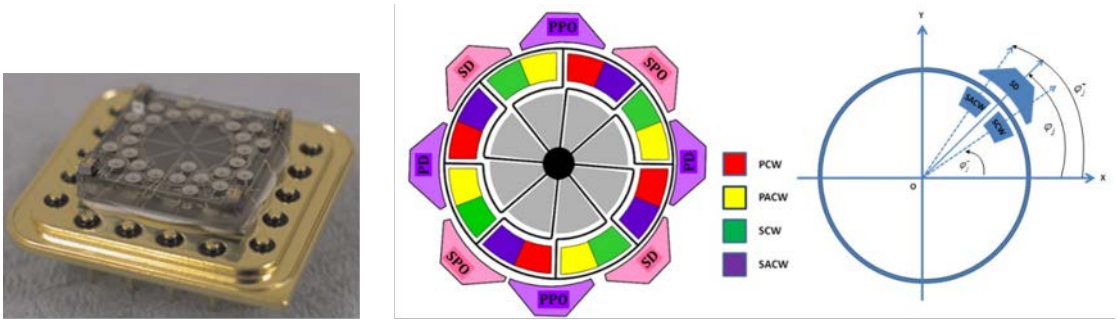

Fig. 1, (a), Vacuum packaged gyro device, (b), Schematic of micro-ring vibrating gyroscope. (c), the pair of tuning electrodes for SD mode.

2.1 Model in physical coordinate system

Neglecting influences of the centrifugal and angular acceleration forces, the simplified equations of motion for the in-plane flexural vibrations of order n=2 can be modelled by a generalized two dimensional oscillator coupled with damping and stiffness imperfections, and rate induced Coriolis force. The equation of motion is:

$$\ddot{\underline{q}} + \{[C] + [G]\}\dot{\underline{q}} + [K]\underline{q} = \underline{F} \tag{1}$$

Here vector $\underline{q} = \begin{bmatrix} x \\ y \end{bmatrix}$ represents the displacements of vibration, and $\underline{F} = \begin{bmatrix} f_x/m_x \\ f_y/m_y \end{bmatrix}$ denotes acceleration imposed by external forces. $[C]$ and $[G]$ are the damping and gyroscopic matrices, and $[K]$ denotes the stiffness matrix including the electrostatic stiffness correction matrix $[K_E]$:

$$[C] = 2\vartheta_0\omega_0\begin{bmatrix} 1+\gamma_1 & \gamma_2 \\ \gamma_2 & 1-\gamma_1 \end{bmatrix};\ [G] = 2\begin{bmatrix} 0 & \Omega_z \\ -\Omega_z & 0 \end{bmatrix};\ [K] = {\omega_0}^2\begin{bmatrix} 1+\mu_1 & \mu_2 \\ \mu_2 & 1-\mu_1 \end{bmatrix} + [K_E] \tag{2}$$

The natural frequency of the perfect ring is ω_0 and ϑ_0 is the average damping ratio. The terms γ_1, γ_2 and μ_1, μ_2 are the damping and stiffness perturbations from the ideal. Ω_z is the applied angular rate that introduces Coriolis force to both modes. The gyroscope device used here is packaged in vacuum that allows a high Q factor of more than 20000. The electrostatic stiffness correction $[K_E]$ is designed to cancel the stiffness imperfections explicitly denoted by μ_1 and μ_2. The electrostatic correction can be accurately controlled by the tuning voltages. The detailed deduction of the electrostatic spring softening effect from all the 16 tuning electrodes is presented in the next section.

The transfer function approach is well suited for the analysis of forced vibration. Here, it is used to describe the automated "coarse" tuning procedure for removing the large stiffness imperfections. In the absence of rotation, the frequency response function matrix $H = \begin{bmatrix} H_{dd} & H_{ds} \\ H_{sd} & H_{ss} \end{bmatrix}$ with displacement vector $\underline{q}$ as output and external forces $\underline{F}$ as input is readily induced from the inverse of the dynamic stiffness matrix, which is described as

$$\begin{aligned} D &= \mathrm{S}^2[I] + \mathrm{S}[C] + [K] \\ &= \begin{bmatrix} S^2 + 2\vartheta_0\omega_0(1+\gamma_1)S + {\omega_0}^2(1+\mu_1) & 2\vartheta_0\omega_0\gamma_2 S + {\omega_0}^2\mu_2 \\ 2\vartheta_0\omega_0\gamma_2 S + {\omega_0}^2\mu_2 & S^2 + 2\vartheta_0\omega_0(1-\gamma_1)S + {\omega_0}^2(1-\mu_1) \end{bmatrix} \end{aligned} \tag{3}$$

Without rate input, the transfer function describing the cross coupling between the two modes is:

$$H_{sd} = \frac{-2\vartheta_0\omega_0\gamma_2 s-{\omega_0}^2\mu_2}{s^4+4\vartheta_0\omega_0 s^3+\left[2{\omega_0}^2+4{\vartheta_0}^2{\omega_0}^2(1-{\gamma_1}^2-{\gamma_2}^2)\right]s^2+4\vartheta_0{\omega_0}^3(1-\gamma_1\mu_1-\gamma_2\mu_2)s+{\omega_0}^4(1-{\mu_1}^2-{\mu_2}^2)} \quad (4)$$

In the rate mode, only the primary mode is excited by F_x, the transfer function describing the primary mode response with respect to excitation F_x is given by:

$$H_{dd} = \frac{s^2+2\vartheta_0\omega_0(1-\gamma_1)s+{\omega_0}^2(1-\mu_1)}{s^4+4\vartheta_0\omega_0 s^3+\left[2{\omega_0}^2+4{\vartheta_0}^2{\omega_0}^2(1-{\gamma_1}^2-{\gamma_2}^2)\right]s^2+4\vartheta_0{\omega_0}^3(1-\gamma_1\mu_1-\gamma_2\mu_2)s+{\omega_0}^4(1-{\mu_1}^2-{\mu_2}^2)} \quad (5)$$

The transfer function model is used for the "coarse" mode tuning. The phase responses provided by these two transfer functions are used to develop a closed loop form of mode tuning to remove the large part of the stiffness imperfections. The procedure is described in section 4.

2.2 Time averaged model in elliptic coordinate system

The accuracy of mode tuning when the gyro is operating in rate mode is restricted by the damping imperfections that causes an additional response at the sense mode. It is difficult to separate the response caused by the cross damping term from that caused by the stiffness cross term. This limitation can be mitigated by operating the gyroscope in the rate integrating mode. The motion analysis of the RIG is more convenient by expressing the equation of motion in terms of amplitude and phase, instead of rectangular coordinates as in equations (1) and (2). Transformation of the equation of motion from rectangular coordinates to time averaged elliptical polar coordinates has been described in detail in [29][30].

The equation of motion in the Cartesian coordinate system with state variables as displacement and velocity of vibration as $u = [x \quad y \quad \dot{x} \quad \dot{y}]^T$. The coordinate transformation expresses the system equation in terms of slow time varying orbital elements described in figure 2. State variables are defined as $z = [a \quad b \quad \theta \quad \varphi]'$. Here φ denotes the phase shift between the resultant drive f_a and response component $a(t)$ in the major axis. The transformation from state vector u in the rectangular coordinate system to state vector z in the elliptic polar coordinate system is described as

$$\begin{cases} x(t) = a\cos\theta\cos(\omega t+\varphi) - b\sin\theta\sin(\omega t+\varphi) \\ y(t) = a\sin\theta\cos(\omega t+\varphi) + b\cos\theta\sin(\omega t+\varphi) \\ \dot{x}(t) = \omega(-a\cos\theta\sin(\omega t+\varphi) - b\sin\theta\cos(\omega t+\varphi)) \\ \dot{y}(t) = \omega(-a\sin\theta\sin(\omega t+\varphi) + b\cos\theta\cos(\omega t+\varphi)) \end{cases} \quad (6)$$

Equation (1) can be rewritten in terms of the slow time varying orbital elements using the transformation defined by equation (6).

$$\dot{a} = -av_0\omega_0(1+\gamma_1\cos 2\theta+\gamma_2\sin 2\theta) - \frac{1}{2}b\omega_0(\mu_1\sin 2\theta - \mu_2\cos 2\theta) + f_a \quad (7)$$

$$\dot{b} = -bv_0\omega_0(1-\gamma_1\cos 2\theta-\gamma_2\sin 2\theta) + \frac{1}{2}a\omega_0(\mu_1\sin 2\theta - \mu_2\cos 2\theta) + f_b \quad (8)$$

$$\dot{\theta} = -\Omega_z + \frac{a^2+b^2}{a^2-b^2}v_0\omega_0(\gamma_1\sin 2\theta-\gamma_2\cos 2\theta) - \frac{ab}{a^2-b^2}\omega_0(\mu_1\cos 2\theta + \mu_2\sin 2\theta) + f_\theta \quad (9)$$

$$\dot{\varphi} = \frac{1}{2}\omega_0\frac{a^2+b^2}{a^2-b^2}(\mu_1\cos 2\theta + \mu_2\sin 2\theta) + \frac{ab}{a^2-b^2}2v_0\omega_0(-\gamma_1\sin 2\theta+\gamma_2\cos 2\theta) + \omega_0 - \omega + f_\phi \quad (10)$$

Where $f_a, f_b, f_\theta, f_\phi$ are effective forces on the elliptic elements caused by f_x, f_y, and have the form of proportional velocity and skew symmetric displacement feedback [11][12] for energy sustain and quad nulling respectively. Control forces f_x, f_y are described by

$$\begin{bmatrix} f_x \\ f_y \end{bmatrix} = \beta \begin{bmatrix} 1 & 0 \\ 0 & 1 \end{bmatrix} \begin{bmatrix} \dot{x} \\ \dot{y} \end{bmatrix} + \alpha \begin{bmatrix} 0 & 1 \\ -1 & 0 \end{bmatrix} \begin{bmatrix} x \\ y \end{bmatrix} \tag{11}$$

When the orbit phase shift φ is maintained at zero by the resonance tracking control, the effective forces in the elliptic frame are described as:

$$\begin{cases} f_a = \frac{1}{2} a\beta - \frac{1}{2\omega} b\alpha \\ f_b = \frac{1}{2} b\beta - \frac{1}{2\omega} a\alpha \\ f_\theta = 0 \\ f_\phi = 0 \end{cases} \tag{12}$$

In order to implement the feedback controls in the elliptic coordinate system, it is necessary to accurately measure the four state variables. The capacitive sensing circuit measures the displacement of the two vibration modes $x(t), y(t)$. Each of the vibration signals is decomposed into a pair of in-phase and quadrature components via a digital signal orthogonal demodulation process described by:

$$\begin{cases} x(t) = C_x \cos(\omega t) + S_x \sin(\omega t) \\ y(t) = C_y \cos(\omega t) + S_y \sin(\omega t) \end{cases} \tag{13}$$

The demodulation results C_x, S_x, C_y, S_y are slow time varying compared with the displacements, and they have significantly less noise due to the low pass filtering used in the narrow band demodulation process. The slow time-varying variables of the vibration, the amplitudes a, b, phase φ and precession angle θ, are readily calculated from the demodulation results C_x, S_x, C_y, S_y as described in [30][31].

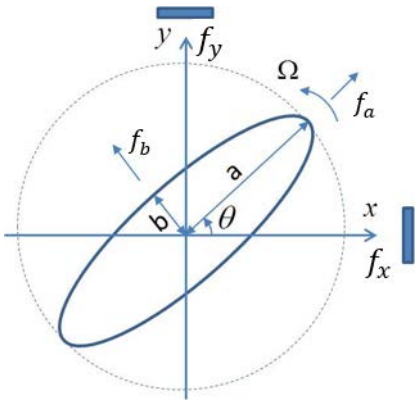

Figure 2. The general elliptic orbit and precession of two-dimensional oscillator.

Equation (8) shows that the major cause of developing quad amplitude b is due to stiffness imperfections including frequency mistuning and modal spring coupling. In the absence of quad nulling control, minimal b indicates the stiffness imperfection terms μ_1, μ_2 are minimized and the modes are well matched. For a well-tuned device, if no quad nulling is required, the quad signal b can be used as an indirect measurement of mistuning and as a feedback term for the real time dynamic tuning control. In this paper, we propose to use the resonance tracking described by equation (10) for high precision mode tuning. When the amplitude of the minor axis b is suppressed to zero, the effect of damping imperfections γ_1, γ_2 on the tracked resonance frequency is negligible. The stiffness imperfections μ_1, μ_2 can be assessed by checking the resonance frequency deviation from the average at precession angle $\theta = 0$ and $\theta = \frac{\pi}{4}$ respectively.

3. Decoupled electrostatic trimming

High precision mode tuning needs to deal with both the diagonal and cross stiffness imperfection terms denoted as μ_1, μ_2 in the stiffness matrix. Figure 1(b) shows the tuning electrode arrangement. Instead of using the conventional sixteen electrodes arrangement [4], this device employs eight electrodes outside of the ring for the purposes of drive and sensing of vibration. It has the advantage of increased electromechanical coupling factor for both excitation and sensing, and maximum electrostatic tuning range from using the whole interior space of the ring. However, the stiffness correction from the four tuning voltages are coupled. This section briefly describes how the electrostatic stiffness can be decoupled so that independent modification of both the cross and diagonal terms of the stiffness matrix is possible. Detailed description of the principle of electrostatic tuning for ring type gyroscope and the related decoupling algorithm can be found in our previous work [3][20].

There are 8 pairs of tuning electrodes lay inside the ring resonator. Figure 1(c) shows one pair of tuning electrodes SCW and SACW for the secondary mode. The electrodes are defined by the angular location of the electrode φ_j, its arc length α. The location of corresponding tuning electrodes are $\varphi_j^+ = \varphi_j + \alpha$, and $\varphi_j^- = \varphi_j - \varphi$, and the locations of these tuning electrodes are located at $\varphi_j = 0, \frac{\pi}{4}, \frac{\pi}{2}, \frac{3\pi}{4}, \pi, \frac{5\pi}{4}, \frac{3\pi}{2}, \frac{7\pi}{4}$. The stiffness correction matrix from one pair of tuning electrodes [19] is described as

$$[K]_j = [K]_j^+ + [K]_j^- = \frac{\varepsilon_0 ad}{2h_0^3} V_{j^-\Delta}^2 \begin{bmatrix} 2\alpha + \frac{1}{n}\sin 2n\alpha \cos 2n\varphi_j \cos 2n\alpha & -\frac{1}{2n}\sin 2n\alpha \cos 2n\varphi_j \sin 2n\alpha \\ -\frac{1}{2n}\sin 2n\alpha \cos 2n\varphi_j \sin 2n\alpha & 2\alpha - \frac{1}{n}\sin 2n\alpha \cos 2n\varphi_j \cos 2n\alpha \end{bmatrix} + \frac{\varepsilon_0 ad}{2h_0^3} V_{j^-\Delta}^2 \begin{bmatrix} 2\alpha + \frac{1}{n}\sin 2n\alpha \cos 2n\varphi_j \cos 2n\alpha & -\frac{1}{2n}\sin 2n\alpha \cos 2n\varphi_j \sin 2n\alpha \\ -\frac{1}{2n}\sin 2n\alpha \cos 2n\varphi_j \sin 2n\alpha & 2\alpha - \frac{1}{n}\sin 2n\alpha \cos 2n\varphi_j \cos 2n\alpha \end{bmatrix} \quad (14)$$

Here, n=2 is mode number, ε_0 is the permeability in air, h_0 is the nominal gap between the ring and the tuning electrode, and d is the thickness of the ring. $V_{j^+\Delta}$ and $V_{j^-\Delta}$ are voltage differences between the two tuning electrodes and DC bias of the resonator.

The total electrostatic stiffness correction matrix $[K_E]$ is obtained by summing the contributions from all the 8 pairs of tuning electrodes. The components of the stiffness correction matrix $[K_E]$ are given by:

$$K_{11} = 2\beta\alpha\left(V_{M1}^{+\,2} + V_{M1}^{-\,2} + V_{M2}^{+\,2} + V_{M2}^{-\,2}\right) + \beta\frac{1}{n}\sin 2n\alpha \cos 2n\alpha \left(V_{M1}^{+\,2} + V_{M1}^{-\,2} - V_{M2}^{+\,2} - V_{M2}^{-\,2}\right) \quad (15)$$

$$K_{21} = K_{12} = \beta\frac{1}{2n}\sin 2n\alpha \cos 2n\alpha \left(V_{M1}^{+\,2} - V_{M1}^{-\,2} - V_{M2}^{+\,2} + V_{M2}^{-\,2}\right) \quad (16)$$

$$K_{22} = 2\beta\alpha\left(V_{M1}^{+\,2} + V_{M1}^{-\,2} + V_{M2}^{+\,2} + V_{M2}^{-\,2}\right) - \beta\frac{1}{n}\sin 2n\alpha \cos 2n\alpha \left(V_{M1}^{+\,2} + V_{M1}^{-\,2} - V_{M2}^{+\,2} - V_{M2}^{-\,2}\right) \quad (17)$$

Here V_{M1}^+ V_{M1}^- V_{M2}^+ V_{M2}^- are the voltage differences between each tuning electrode groups PCW, PACW, SCW and SACW and the DC bias respectively. The complete electrostatic stiffness matrix can be written as:

$$[K_E] = \begin{bmatrix} \rho_1(A_1 + A_2) + \rho_2(A_1 - A_2) & \rho_3(B_1 - B_2) \\ \rho_3(B_1 - B_2) & \rho_1(A_1 + A_2) - \rho_2(A_1 - A_2) \end{bmatrix} \quad (18)$$

where

$$\beta = \frac{\varepsilon_0 ad}{2{h_0}^3},\ \rho_1 = 2\beta\alpha,\ \rho_2 = \frac{\beta}{n}\sin 2n\alpha \cos 2n\alpha,\quad \rho_3 = \frac{\beta}{2n}\sin 2n\alpha \cos 2n\alpha \quad (19)$$

and

$$\begin{cases} A_1 = {V_{M1}^+}^2 + {V_{M1}^-}^2 \\ B_1 = {V_{M1}^+}^2 - {V_{M1}^-}^2 \\ A_2 = {V_{M2}^+}^2 + {V_{M2}^-}^2 \\ B_2 = {V_{M2}^+}^2 - {V_{M2}^-}^2 \end{cases} \tag{20}$$

Equation (20) reveals that the effective stiffness correction is proportional to the square of tuning voltages, and shows there are voltage couplings between the stiffness correction terms A_1 and B_1, and A_2 and B_2 respectively. Therefore, the tunings of diagonal and cross stiffness terms as described in equation (**18**) are coupled. It requires a decoupling algorithm to calculate the tuning voltages V_{M1}^+ V_{M1}^- V_{M2}^+ V_{M2}^-, so that the right corrections for the direct and cross terms in the system stiffness matrix (18) can be made independently. If $\Delta\mathrm{A}$ denotes the amount of correction required for the diagonal term in the stiffness matrix via A_1, a simple decoupling algorithm for calculating the required tuning voltages V_{M1}^+ and V_{M1}^- based on the current values of A_1 and B_1 is given by:

$$\mathrm{V_{M1}^+} = \frac{\sqrt{(\mathrm{A_1}+\Delta\mathrm{A})+\mathrm{B_1}}}{2}\ ,\ \mathrm{V_{M1}^-} = \frac{\sqrt{(\mathrm{A_1}+\Delta\mathrm{A})-\mathrm{B_1}}}{2} \tag{21}$$

The voltages V_{M1}^+ and V_{M1}^- calculated using algorithm (21) only changes the diagonal term via A_1. The cross tuning term B_1, although related to V_{M1}^+ and V_{M1}^-, is not changed. Similarly, any modification $\Delta\mathrm{B}$ can be made to the cross terms of stiffness matrix via B_1 independently by trimming tuning voltages V_{M1}^+ and V_{M1}^- simultaneously according to (21). The same decoupling algorithm applies to A_2 and B_2 that doubles the tuning range.

4. Closed-loop "coarse" mode tuning

Despite the high precision machining or microfabrication methods used in manufacture of high performance gyroscope the level of structural imperfection remaining post fabrication is still too large for satisfactory performance as a rate integrating gyroscope. In the case of the MEMS gyroscope studied in this body of research the frequency split is 1.4Hz, and cross-coupling induced non-driven response at the secondary mode is 25% of the primary mode response. The total damping fluctuation from the average is 3%. Clearly the cross-coupling is dominated by the stiffness imperfections. This section describes a closed loop "coarse" mode tuning scheme conducted in rate mode. The primary mode is excited at its resonance frequency ω_{x} with its vibration amplitude maintained constant. Initially the stiffness imperfections μ_1, μ_2 dominate the cross-coupling between the modes and must be reduced first before addressing damping imperfections γ_1, γ_2 as part of a subsequent compensation scheme

The proposed "coarse" mode tuning consists of two steps. In the first step, only the primary mode is excited at resonance and it's amplitude maintained constant. With zero rate input to the gyroscope, the response of the secondary mode is due to cross-coupling caused by the damping and stiffness cross terms γ_2, μ_2. The amplitude and phase responses are described by the cross-coupling frequency response function described by equation (4). The phase shift of the secondary mode response with respect to the drive mode response is expressed as:

$$\Delta\varphi_c(s) = \angle H_{sd} - \angle H_{dd} = \ \angle(-2\vartheta_0\omega_0\gamma_2 s - {\omega_0}^2\mu_2) - \angle\{s^2 + 2\vartheta_0\omega_0(1-\gamma_1)s + {\omega_0}^2(1-\mu_1)\} \tag{22}$$

Neglecting the influence of the damping imperfections since they are small compared to the stiffness imperfections, the resonant frequencies for the primary and secondary modes are approximately given by:

$$\omega_x = \omega_0\sqrt{\left(1-\sqrt{{\mu_1}^2+{\mu_2}^2}\right)}\ ,\ \omega_y = \omega_0\sqrt{\left(1+\sqrt{{\mu_1}^2+{\mu_2}^2}\right)} \tag{23}$$

Figure 3 shows the phase shift $\Delta\varphi_c$ versus stiffness cross coupling μ_2 when the primary mode is driven at it's resonance frequency ω_x. Clearly when $\mu_2 > 0$ then $\Delta\varphi_c > 0$. Similarly when $\mu_2 < 0$ then $\Delta\varphi_c < 0$. As $\mu_2 \rightarrow$

0 , the phase shift $\Delta\varphi_c$ changes very rapidly between leading and lagging phases. The reduction of cross coupling μ_2 is conducted by minimizing the response amplitude of the secondary mode. The direction of change made to μ_2 electrostatically is indicated by the phase shift $\Delta\varphi_c$. Note that a small part of the secondary mode response is caused by the cross coupling due to the damping term γ_2, on which electrostatic softening has no effect. Therefore, the amplitude of the secondary mode response cannot be made zero by electrostatic trimming of μ_2.

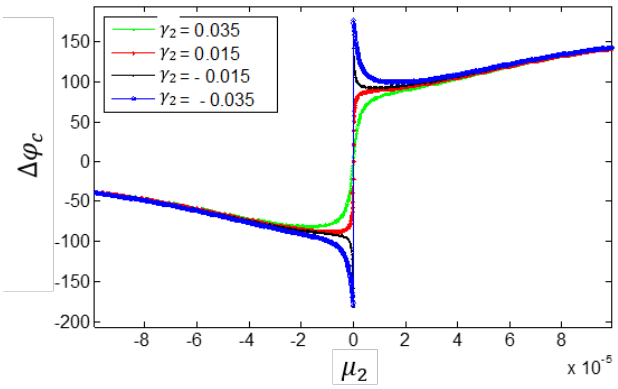

Figure 3. Simulated phase delay of the secondary mode relative to the primary mode response.

The closed loop tuning procedure for μ_2 is shown in the block diagram figure 4. Reduction of μ_2 is performed electrostatically according to the sign of the phase shift $\Delta\varphi_c$. Note that as $\mu_2 \to 0$, $\Delta\varphi_c$ becomes singular in the absence of cross damping imperfections. For the general case where $\gamma_2 \neq 0$ then as $\mu_2 \to 0$ the damping cross term γ_2 introduces a phase shift of $\tan^{-1}\left(\frac{\gamma_2}{\mu_2 Q}\right)$. This results in a small tuning error on μ_2.

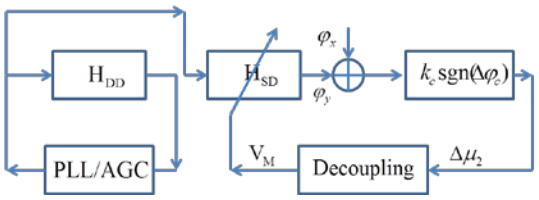

Figure 4. Closed-loop form electrostatic tuning of cross coupling μ_2

The second step of the "coarse" mode tuning procedure removes the diagonal term μ_1 in the stiffness imperfection matrix. Cross-coupling between the two vibration modes is negligible after the stiffness cross coupling μ_2 is minimized in the first step of mode tuning. The diagonal term μ_1 can be readily assessed by the phase difference between the responses of the two vibration modes by exciting the secondary mode with the same signal that drives the primary mode into resonance. The phase difference is calculated using transfer functions H_{dd} and H_{ss} described in section 2.

$$\Delta\varphi_d(s) = \angle\{s^2 + 2\vartheta_0\omega_0(1-\gamma_1)s + {\omega_0}^2(1-\mu_1) - (2\vartheta_0\omega_0\gamma_2 s + {\omega_0}^2\mu_2)\} \tag{24}$$

$$- \angle\{s^2 + 2\vartheta_0\omega_0(1+\gamma_1)s + {\omega_0}^2(1+\mu_1) - (2\vartheta_0\omega_0\gamma_2 s + {\omega_0}^2\mu_2)\}$$

The task of mode tuning at this step is to minimize the phase difference $\Delta\varphi_d$ at resonance frequency ω_x of the primary mode by electrostatically eliminating μ_1. The phase difference at resonance frequency ω_x is described as:

$$\Delta\varphi_d(\omega_x) = \tan^{-1}\frac{2\vartheta_0\omega_0(1-\gamma_1-\gamma_2)\omega_x}{-{\omega_x}^2 + {\omega_0}^2(1-\mu_1-\mu_2)} - \tan^{-1}\frac{2\vartheta_0\omega_0(1+\gamma_1-\gamma_2)\omega_x}{-{\omega_x}^2 + {\omega_0}^2(1+\mu_1-\mu_2)}$$

$$= \tan^{-1}\frac{2\vartheta_0(1-\gamma_1-\gamma_2)\sqrt{1-\sqrt{{\mu_1}^2+{\mu_2}^2}}}{\sqrt{{\mu_1}^2+{\mu_2}^2}-\mu_1-\mu_2} - \tan^{-1}\frac{2\vartheta_0(1+\gamma_1-\gamma_2)\sqrt{1-\sqrt{{\mu_1}^2+{\mu_2}^2}}}{\sqrt{{\mu_1}^2+{\mu_2}^2}+\mu_1-\mu_2} \quad (25)$$

Since the stiffness cross coupling $\mu_2 \approx 0$, then

$$\Delta\varphi_d \approx \frac{\pi}{2} - \tan^{-1}\frac{2\vartheta_0(1+\gamma_1-\gamma_2)\sqrt{1-\mu_1}}{2\mu_1} \quad (26)$$

From equation (26), it is clear that when μ_1 is electrostatically compensated, the two response signals corresponding to the primary and sense modes are in-phase such that $\Delta\varphi_d = 0$.

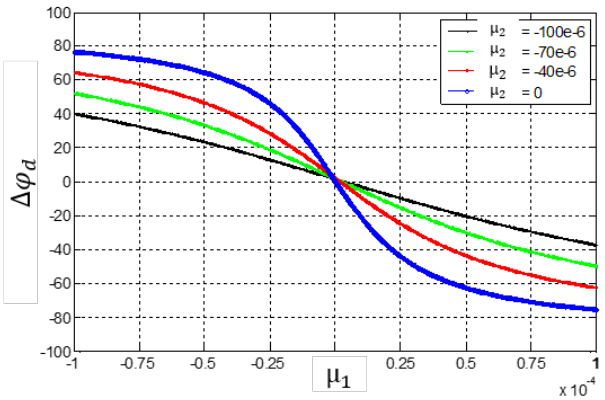

Figure 5. Phase difference between responses of the two vibration modes versus imperfection term μ_1.

The phase difference $\Delta\varphi_d$ described by equation (26) is used to determine the direction of electrostatic correction. As shown in figure 5 of the simulated plot of the phase difference $\Delta\varphi_d$ versus imperfection term μ_1, μ_1 needs to be trimmed down when phase $\Delta\varphi_d$ is negative, otherwise, μ_1 should be trimmed up if $\Delta\varphi_d$ is positive. This algorithm works even in the presence of small amount of cross coupling μ_2. In practical implementation of the tuning process based on a DSP platform, instead of directly calculating phase difference $\Delta\varphi_d$, the quadrature component of the sense mode response is used as a measure of the phase difference. The closed loop tuning procedure for μ_1 is described in block diagram figure 6. It is implemented by minimizing the quadrature component of the secondary mode response with the drive signal as the reference for signal demodulation. The closed loop form tuning procedure ensures the quadrature component of the sense mode reaches zero, therefore $\Delta\varphi_d = 0$. However, at this stage, the frequency mismatch $\mu_1$is not completely zero due to effects from the damping imperfections. There is a small residual frequency mismatch $\mu_1$that cannot be removed in rate mode.

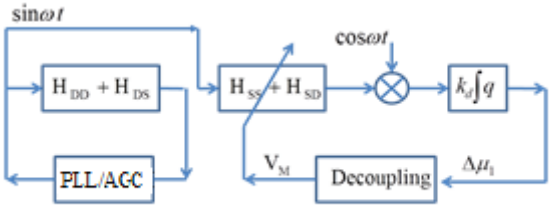

Figure 6, Block diagram of closed loop form tuning for removing imperfection term μ_1.

5. Precision tuning in whole angle mode

The lower limit of the mode tuning described in section 4 is determined by the damping imperfections γ_1, γ_2. In the gyro rate mode it is difficult to separate the effect of damping imperfections from the effect of the stiffness imperfections. This section proposes a high precision mode tuning in the rate integrating mode where the contributions from damping and stiffness imperfections are readily separated. This will extend the lower limit of tuning beyond that possible in rate operating mode. A prerequisite is that the "coarse" mode tuning must have sufficiently reduced $\mu_1,\ \mu_2$, so that the gyro can be controlled to operate as a whole angle gyro without excessive input rates.

Equation (8) describes the dynamics of the developing minor axis $b(t)$ of the elliptic trajectory of vibration caused by residual mistuning $\mu_1,\ \mu_2$ when the major axis $a(t)$ is stabilized. Quad nulling is present only to compensate the imperfections $\mu_1,\ \mu_2$ causing angle drift. It provides a way to identify the residual mistuning terms $\mu_1,\ \mu_2$. Without quad nulling, the solution to equation (8) is given by

$$b(t) = \frac{a}{2\upsilon_0}\frac{(\mu_1 \sin 2\theta - \mu_2 \cos 2\theta)}{(1-\gamma_1 \cos 2\theta - \gamma_2 \sin 2\theta)}(1 - e^{-ct}) \tag{27}$$

Here $c = \upsilon_0\omega_0(1 - \gamma_1 \cos 2\theta - \gamma_2 \sin 2\theta)$ is the damping modulated by angular precession. It determines the time constant of the transient process of $b(t)$. For the gyroscope used in this study, the quality factor is measured to be 22000, and the resonant frequency is 14 kHz. The time constant is 2 seconds. The damping imperfection is measured to be less than 3 percent [11]. When the gyro is operated as an angle gyro with a constant rate input of 15 degrees per second, the developing quadrature has a period of 24 seconds. Equation (27) can be approximate to

$$b(t) \approx \frac{a}{2\upsilon_0}(\mu_1 \sin 2\theta - \ \mu_2 \cos 2\theta) \tag{28}$$

Stiffness imperfections $\mu_1,\ \mu_2$ can be approximately evaluated by:

$$\mu_1 = \frac{2\upsilon_0}{a}\ b, \ \text{ when } \ \theta = \frac{\pi}{4} \tag{29}$$

$$\mu_2 = -\frac{2\upsilon_0}{a}\ b, \ \text{ when } \ \theta = 0 \tag{30}$$

Alternatively, the mistuning $\mu_1,\ \mu_2$ can be identified using equation (10), which governs the resonance frequency of the RIG. With quad nulling control in place, the amplitude of the minor axis $b(t)$ is suppressed to close to zero. The effect of the damping imperfection terms γ_1, γ_2 on the resonance frequency is negligible. The actual frequency tracked by the PLL is simplified as:

$$\omega = \omega_0\left(1 + \frac{1}{2}(\mu_1 \cos 2\theta + \ \mu_2 \sin 2\theta)\right) \tag{31}$$

It shows the operating resonance frequency being modulated by the angular precession around the nominal frequency ω_0. For the purpose of evaluating the stiffness imperfections $\mu_1,\ \mu_2$ from the recorded resonance frequency modulation pattern when the gyroscope undergoes continuous rotation, the nominal resonance frequency ω_0 is readily removed by a zero phase shift high pass filter.

$$\tilde{\omega} = \frac{1}{2}\omega_0(\mu_1 \cos 2\theta + \ \mu_2 \sin 2\theta) \tag{32}$$

Equation (32) provides an accurate, direct evaluation of frequency split between the two vibration modes. It also provides a means for extracting mistuning $\mu_1,\ \mu_2$ from the frequency deviation at angles $\theta = 0$ and $\theta = \frac{\pi}{4}$ respectively. In practical applications, instead of calculating the exact values of the mistuning $\mu_1,\ \mu_2$, (32) gives the direction of trimming so that the mode tuning can be implemented recursively.

6. Experimental results

This section describes the closed-loop control necessary for the operation of the rate integrating gyroscope, and all the experimental test results conducted for precision mode tuning based on the real time control system. The experimental setup is shown in figure 7, which is capable of RIG testing with an external continuous rate input up to 300 rpm.

Figure 7, Experimental setup for the rate integrating gyroscope.

6.1 Control platform

The mode tuning is incorporated onto a DSP based gyroscope control system. The system block diagram is shown in figure 8. The signal generation is based on an audio codec chip with 192 KHz sampling rate and the principle of direct digital synthesis technique (DDS) is used to create high quality sine/cosine waves for resonance excitations. The frequency resolution is 0.3 mHz. It also provides the digital reference for orthogonal detection. The digital orthogonal demodulation plays a key role to resolve the in-phase and quadrature components of the input vibrations signals, which are used to calculate the amplitude and phase information of both the primary and sense modes, and to provide the reconstructions of displacement and velocity signals for real time dynamic control. The measurement results are of high precision and low noise because of the narrow band detection technique employed.

Voltages applied to the four groups of electrostatic mode tuning are controlled by a 4 channel 16bit DAC. They are amplified to provide the full range of tuning voltages up to the DC bias of 25 volts. This gives a voltage resolution of 0.38 mV. The controller can be readily switched between rate mode and rate integrating mode. The control for RIG consists of four modules: (1) Resonance frequency tracking based on a PLL; (2) Energy sustain by velocity feedback to maintain a constant amplitude of the major axis of the elliptic trajectory; (3) Quad nulling based on an anti-skew displacement feedback to supress the minor axis; (4) State feedback to compensate damping and stiffness imperfections. System states, the velocity and displacement, for feedback control are recreated using the demodulation results C_x, S_x, C_y, S_y and the digital signal reference.

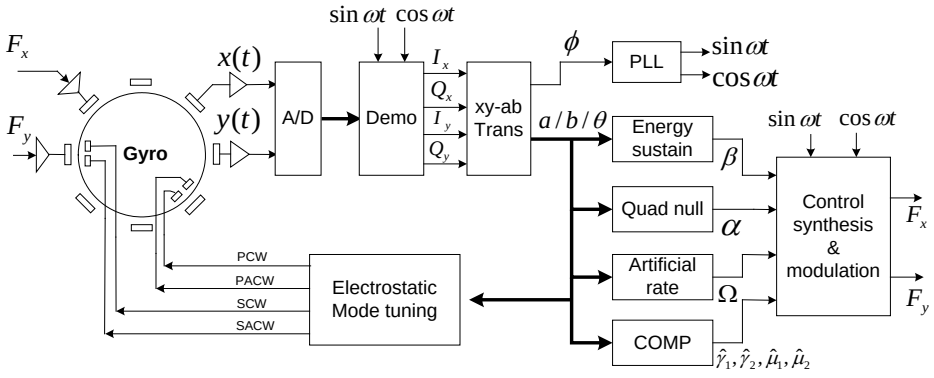

Figure 8, Block diagram of the gyroscope control system.

6.2 Initial cross coupling and mistuning

The DC bias of the gyroscope is set at 25 V and all the four groups of tuning voltages are set at half way the DC bias before the electrostatic tuning procedure begins. Four frequency response tests corresponding to the transfer functions $\mathrm{H_{DD}}, \mathrm{H_{DS}}, \mathrm{H_{SS}}, \mathrm{H_{SD}}$ are shown in figure 9. It shows that the cross coupling induced non-driven response at the secondary mode is 25% of the response of the driven primary mode, and the frequency split is 1.4Hz.

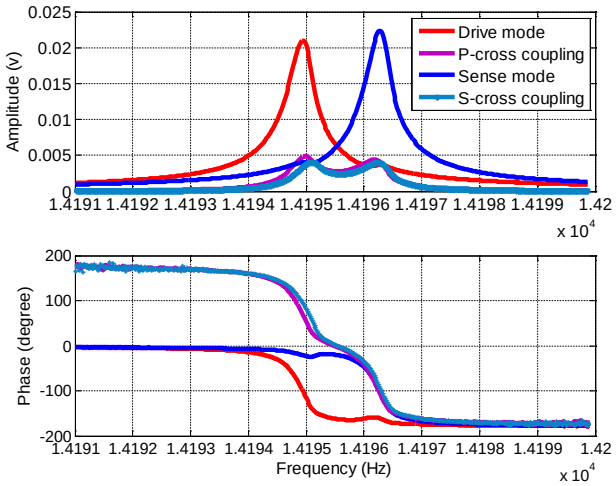

Figure 9. Experimentally obtained full frequency response data around the resonance frequency.

6.3 Tuning results in rate mode

The frequency response data in figure 9 shows that cross coupled response corresponding to $\mathrm{H_{DS}}$ and $\mathrm{H_{SD}}$ are almost identical as expected due to the symmetric stiffness matrix. As described in section 3, cross coupling caused by μ_2 can be removed by adjusting the effective electrostatic tuning term $B_1 - B_2$. The cross coupling caused by the damping imperfection γ_2 cannot be changed electrostatically. However, the effect of cross coupling from γ_2 is suppressed by the high Q factor. For this gyroscope in its initial state $\frac{\gamma_2}{\mu_2} \sim 10^{-6}$.

The reduction of cross coupling is implemented in a closed-loop form. The objective is to bring the phase of the cross coupling signal to be ± 180 degrees relative to the primary mode response, as described in figure 3. The first stage of figure 10 shows that the amplitude of cross coupling response is reduced from 10 mV to 0.3 mV when $B_1 - B_2$ is increased to 250 V^2, as shown in figure 11. Removing cross coupling hardly changes the frequency, as shown in the first stage in figure 10(b).

The diagonal stiffness imperfection term μ_1 is minimized by changing $A_1 - A_2$ from zero to 430 V^2, which is shown in the second stage in figure 11. It shifts the tracked resonance frequency of the primary mode by 0.62 Hz, as shown in the second stage of figure 10. Figure 12 shows the matched modes after the two steps of electrostatic tuning. This mode tuning takes less than 2minutes because of the closed-loop implementation. Figure 12 also shows the residual cross coupling mainly caused by the cross damping imperfection term γ_2. Recall γ_2 is not affected by electrostatic tuning and may ultimately limit the accuracy and stability for those automatic mode tuning algorithms [26][27] conducted in the rate operation mode.

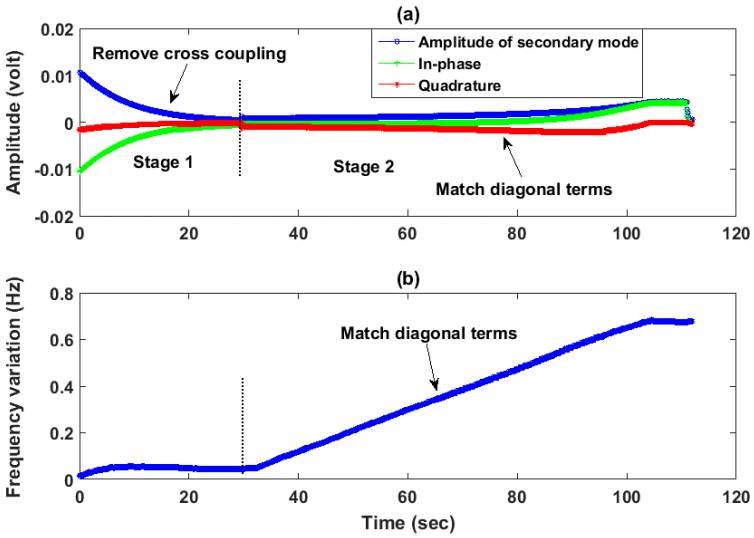

Figure 10. Experimental closed loop tuning process in rate mode, frequency shift away from 14194Hz.

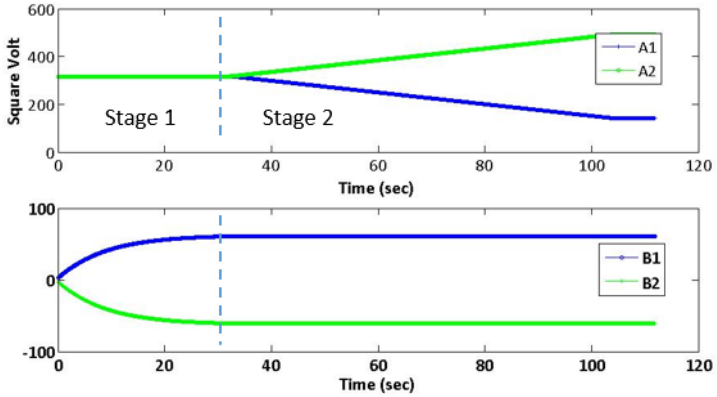

Figure 11. Tuning voltages automatically trimmed: change B1, B2 in stage 1, A1, A2 in stage 2.

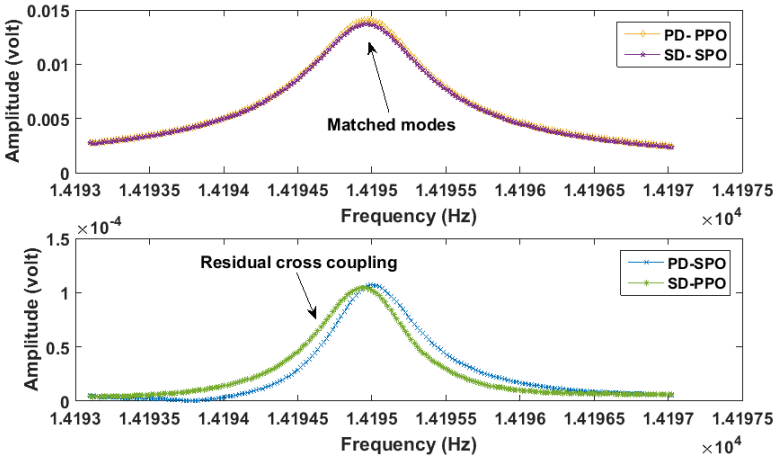

Figure 12. Experimental tests show the matched modes and residual cross coupling mainly caused by damping cross coupling.

6.4 Tuning in whole angle mode

"Fine" tuning in whole angle mode is possible only after the frequency mismatch is reduced sufficiently small in the "coarse" stage. This is because the frequency mismatch determines the rate threshold [15][16], below this input rate the gyroscope stops behaving as a rate integrating gyroscope. Upon completion of the initial tuning with the gyro operating in rate mode the imperfections are sufficiently small to permit further reduction. To observe the imperfections left by the "coarse" tuning stage, the gyroscope must thereafter be operated in rate integrating mode. Figure 13 shows that as the angle precesses, the tracked resonance frequency varies with the rotation angle periodically with a peak to peak value of 40 mHz. This is in agreement with equation (32). The damping is compensated with velocity feedback which has reduced the rate of angle drift to 1.5 °/s. For the following experimental tests, the amplitude of the major axis a as described by equation (7) is stabilized at 25 mV by using the PI energy sustain control loop.

Stiffness imperfection terms μ_1, μ_2 can be evaluated using the unsuppressed quadrature b using equations (29) (30) or from the modulation pattern of the resonance frequency $\tilde{\omega}$ against the precession angle using equation (32). In figure 13, by examining the quadrature values of b at angular positions of $\frac{\pi}{4}$ and 0 respectively, the values of stiffness imperfections after the coarse tuning are estimated to be $\mu_1 > 0$, $\mu_2 \approx 0$. Similar results can be obtained by using the resonance frequency $\tilde{\omega}$ plot in figure 13. These estimations of μ_1, μ_2 are used in the fine tuning in the rate integrating mode.

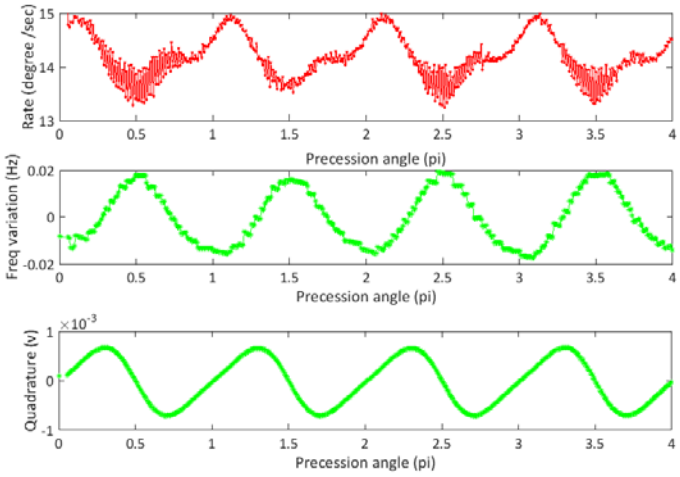

Figure 13. Experimental tests show both amplitude of quadrature and resonance frequency are modulated by precession angle.

The extracted information about the mistuning gives the direction for recursive trimming, either electrostatically or via displacement feedback compensation. Figure 14 shows the frequency split has been reduced from 40 mHz to 10 mHz, and as a result, the amplitude of quadrature is reduced by 5 times without applying quadrature nulling control. When the mistuning becomes smaller, a $\cos 4\theta$ component appears on the quadrature caused by higher order un-modelled dynamics. Figure 15 shows the angular spectrum of the quadrature amplitude and frequency modulation before and after fine tuning. It shows that electrostatic tuning only affects the $\cos 2\theta$ components. The unaffected $\cos 4\theta$ component effectively puts a limit to this proposed tuning method for RIG. This problem may be mitigated by lowering the amplitude of drive for gyroscope devices with higher Q, higher DC bias, or using parametric drive for energy sustain.

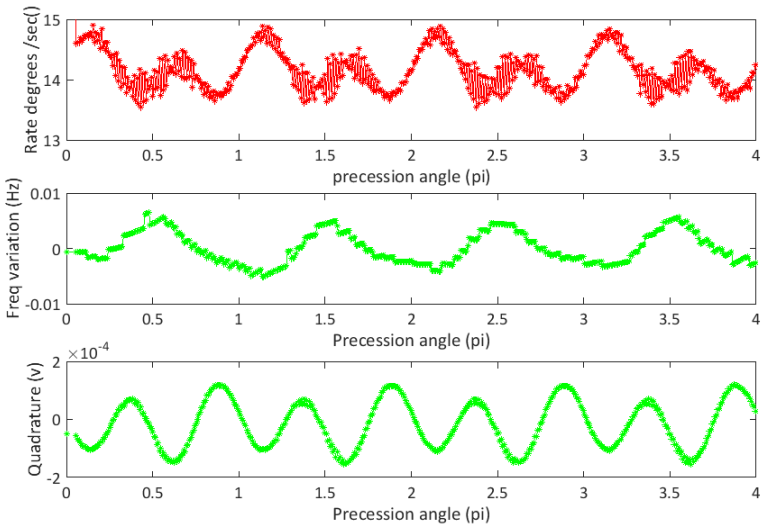

Figure 14. Experimental result shows frequency split is reduced from about 40 mHz to less than 10mHz in whole angle mode.

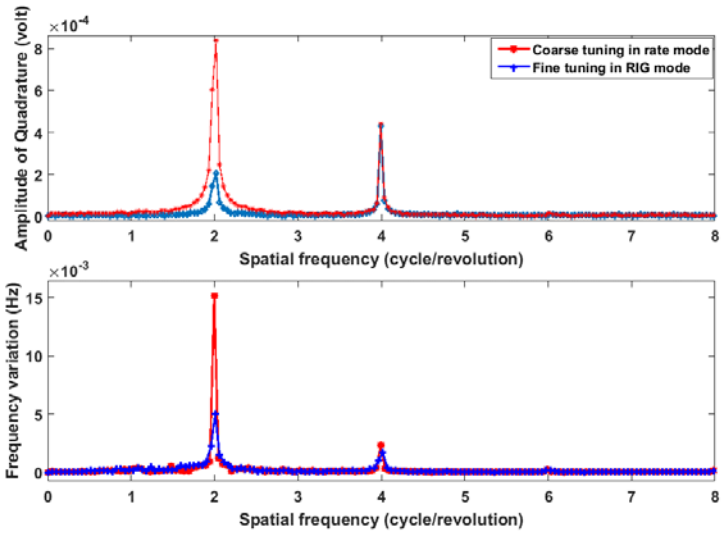

Figure 15, Spectrum analysis of amplitude of quadrature and frequency modulation versus precession angle shows 2th and 4th harmonics.

7. Conclusion

An efficient, high precision electrostatic mode tuning for a MEMS ring type vibratory gyroscope operating in the rate integrating mode is described in this paper. It provides a means for independent trimming of identified cross and diagonal stiffness imperfections based on a decoupling algorithm developed for the ring resonant structure with unique electrodes arrangements. “Coarse” assessment of stiffness imperfections is made firstly in the gyro rate mode by interrogating cross coupling from the primary mode to the secondary mode, and the phase difference between the two modes when they are excited with the same drive signal. Afterwards, precision evaluation of mistuning and frequency split are made by operating the gyroscope in the rate integrating mode, which has the advantages for avoiding the influence of damping imperfections on the estimation of stiffness imperfections. Closed-loop form mode tuning based on the proposed tuning scheme has been implemented, which achieved a frequency split of 40 mHz within 2 minutes. High precision mode tuning

conducted in the whole angle mode improved the accuracy of mode matching to 10 mHz. It also provides an accurate, direct assessment of mode mismatch. Detailed experimental results are provided. All the mode tuning and real time control has been implemented based on a high performance DSP platform.

As the precision of mode tuning is further improved in RIG mode, 4^{th} harmonic components are present in the angle output, quadrature and resonance frequency modulation. This harmonic contamination ultimately defines the tuning accuracy limit of the proposed method. These harmonics are caused by dynamics not included in the conventional gyroscope model.

Acknowledgment

The authors wish to acknowledge the support from K Townsend, C Gregory and A Kazer of UTAS (Plymouth,UK) to this research project in terms of the provision of hardware, and insightful discussions.

Reference

[1]. William Quick. Theory of the vibrating string as an angular motion sensor, *Journal of Applied Mechanics*, vol. 31, no. 3, pp. 523-534, Sep. 1964.

[2]. Mohammad faisal Zaman, Ajit Sharma, Farrokh Ayazi, A mode matched silicon-yaw tuning fork gyroscope with subdegree-per-hour Allan deviation bias instability, *Journal of Microelectromechanical systems*, vol.17, no. 6, pp. 1526-1536, Dec. 2008.

[3]. Barry J. Gallacher, John Hedley, James S. Burdess, Alun James Harris. Electrostatic Correction of Structural Imperfections Present in a Micro ring Gyroscope. *Journal of Microelectromechanical systems*, vol. 14, no. 2, pp. 221-234, April 2005.

[4]. Farrokh Ayazi, Khalil Najafi, A HARPSS Polysilicon Vibrating Ring Gyroscope. *Journal of Microelectromechanical systems*, vol. 17, no. 2, pp169-179, June, 2001.

[5]. P.W. Loveday and C. A. Rogers. The influence of control system design on the performance of vibratory gyroscopes, *Journal of sound and vibration*, vol. 255, no. 3, pp. 417-432, Aug. 2002.

[6]. David Schwartz, Dong Joon Kim, Robert T. M'Closkey, Frequency tuning of disk resonator gyro via mass matrix perturbation, *American Control Conference*, Washington, USA, June 2008, pp. 3740-3745.

[7]. Dennis Kim, Robert M'Closkey, A MEM vibratory gyro with mode-matching achieved by resonator mass loading, *Position, Location and Navigation Symposium - PLANS, 2014 IEEE/ION,* pp.499-503.

[8]. Tsanh-Hung Su, Sarah H. Nitzan, Parsa Taheri-Tehrani, Mitchell H. Kline, Bernhard E. Boser, David A. Horsley. Silicon MEMS Disk Resonator Gyroscope with an Integrated CMOS Analog Front-End. *IEEE SENSORS JOURNAL*, vol. 14, no. 10, pp.3426-3432, Oct. 2014.

[9]. David Rozelle. The Hemispherical Resonator Gyro: From Wineglass to the Planets, *Spaceflight Mechanics*. 2009.

[10]. Doruk Senkal, Mohammed J. Ahamed, Alexander A. Trusov, and Andrei M. Shkel, Achieving Sub-Hz Frequency Symmetry in Micro-Glassblown Wineglass Resonators. *Journal of Microelectromechanical systems*, vol. 23, no. 1, Feb. 2014.

[11]. Z X Hu, B J Gallacher, Control and damping imperfection compensation for a rate integrating MEMS gyroscope, *DGON* Inertial *Sensors and Systems,* Karlsruhe, Germany, Sep. 2015, pp.1-15.

[12]. J. A. Gregory, J. Cho, and K. Najafi, Novel mismatch compensation methods for rate-integrating gyroscopes, *Position, Location and Navigation Symposium - PLANS, 2014 IEEE/ION*, April 2012, pp.252-258.

[13]. Stephen R. Bowles, B.J. Gallacher, Zhongxu Hu, Control scheme to reduce the effect of structural imperfections in a rate integrating MEMS gyroscope. *IEEE sensors journal*, vol. 15, no. 1, pp. 552-560, 2015.

[14]. Painter, C. and Shkel, A, Experimental evaluation of a control system for an absolute angle measuring micromachined gyroscope, *IEEE sensors conference*, Irvine, CA, 2005, pp.1084-1087.

[15]. Igor P. Prikhodko, Jeffrey A. Gregory, Dmitry I. Bugrov, Michael W. Judy, Overcoming limitations of rate integrating gyroscopes by virtual rotation, *IEEE International Symposium on Inertial Sensors and Systems*, Laguna Beach, CA, Feb. 2016.

[16]. B J Gallacher, Principles of a rate integrating gyroscope, *IEEE Transactions on Aerospace and Electronic Systems*, vol.48, no. 1, 2012, pp.658-671.

[17]. David D. Lynch, MRIG Frequency Mismatch and Quadrature Control, IEEE International Symposium on Inertial Sensors and Systems. Laguna Beach, CA. 22-25 Feb. 2014.

[18]. T. Lam and R. B. Darling, Modelling of focused ion beam trimming of cantilever beams, *Proc. 3rd Int. Conf. Modelling and Simulation of Microsystems*, San Diego, CA, Mar. 2000.

[19]. D Joachim and L. Lin, Selective polysilicon deposition for frequency tuning of MEMS resonators, *IEEE Micro Electro Mechanical Systems conference.* Jan. 2002, pp. 728-730.

[20]. Z X Hu, B J Gallacher, A Systematic Approach for Precision Electrostatic Mode Tuning of a MEMS Gyroscope, *Journal of Micromechanics and Microengineering*, vol. 24, oct. 2014, pp.1-15.

[21]. Kimand D J and M'Closkey R T, A systematic method for tuning the dynamics of electrostatically actuated vibrating gyros, *IEEE Transactions on Control Systems Technology,* vol. 14, no. 1, Jan. 2006, pp. 69-81.

[22]. A. Srikantha Phani, Ashwin A. Seshia and Roger T. Howe, Modal coupling in micromechanical vibratory rate gyroscopes, *IEEE Sensors Journal*, vol. 6, no. 5, , Oct. 2006, pp.1144-1152.

[23]. Sangkyung Sung, Woon-Tahk Sung, Young Jae Lee, On the mode-matched control of MEMS vibratory gyroscope via phase-domain analysis and design, IEEE/ASME Trans. on Mechatronics, vol. 14, no. 4, Aug. 2009, pp.446-455.

[24]. Z X Hu, B J Gallacher, Precision mode matching of MEMS gyroscope by *feedback* control, *IEEE sensors*, Limerick, Ireland, Oct. 2011.

[25]. Riccardo Antonello, Roberto Oboe, Automatic mode matching in MEMS vibrating gyroscopes using extremum-seeking control. *IEEE Trans. Industrial Electronics*, vol. 56, no. 10, Oct. 2009, pp. 3880-3891.

[26]. Soner Sonmezoglu, Said Emre Alper, and Tayfun Akin. An Automatically Mode-Matched MEMS Gyroscope with wide and tunable bandwidth, *Journal of Microelectromechanical systems*, vol. 23, no. 2, April 2014, pp.284-297.

[27]. Igor P. Prikhodko, Jeffrey A. Gregory, William A. Clark, John A. Geen, Michael W. Judy, Chae H. Ahn, Thomas W. Kenny. Mode-Matched MEMS Coriolis Vibratory Gyroscopes: Myth or Reality? *Position, Location and Navigation Symposium (PLANS),* 2016 IEEE/ION, April, 2016.

[28]. S. Park and R. Horowitz, Adaptive control for the conventional mode of operation of MEMS gyroscopes, *Journal of Microelectromechanical systems*, vol. 12, no. 1, Feb. 2003, pp.101–108.

[29]. B. Friedland and M.F. Hutton, Theory and error analysis of vibrating-member gyroscope, *IEEE Trans. Automatic Control,* vol. AC-23, no. 4, Aug. 1978, pp.545-556.

[30]. D.D. Lynch, Vibratory Gyro Analysis by the Method of Averaging, *International conference on Gyroscopic Technology and Navigation*, St. Petersburg, 1995.

[31]. IEEE Standard, Specification Format Guide and Test Procedure for Coriolis Vibratory Gyros, *IEEE Std 1431-2004*, Dec. 20 2004, pp.1~78.